nature nanotechnology

Article

https://doi.org/10.1038/s41565-026-02142-z

Picosecond-scale coherent toggle switching of topological spin helicity

Received: 21 December 2024

Accepted: 27 February 2026

Can Liu[1,14], Zefang Li[1,14], Xuange Hu[1,14], Jiangteng Guo[1], Yue Hu[1], Ying Deng[1], Haixue Wang[1], Shaozheng Ji[1], Cuntao Gao[1], Fang Liu[1], Huai Zhang[2], Wei He[3], Tengyu Guo[4], Shaohui Chen[5], Peng-Han Lu[6], Jinxiong Wu[7], Yangfan Hu[5], Zhi-Min Liao[8], Jun-Ming Liu[2,9], Dapeng Yu[10] ✉, Zhipeng Hou[2] ✉, Rafal E. Dunin-Borkowski[6] ✉, Yimei Zhu[11] ✉ & Xuewen Fu[1,12,13] ✉

The switching of conventional magnetization states is a cornerstone of modern spintronics, enabling control over binary ('0' and '1') information bits. Although the coherent control of helicity switching in topological spin configurations is promising for applications such as high-speed multistate memory and neuromorphic and probabilistic computing, realizing it has been challenging. This difficulty stems from the requirement for coherent spin precession while maintaining the intrinsic topology of the spin configurations, which is usually disrupted by conventional excitations. Here we report an experimental realization of coherent helicity toggle switching in nanoscale magnetic vortices occurring on timescales of several hundred picoseconds. This switching behaviour is driven by femtosecond laser pulse excitation under an out-of-plane magnetic field. The mechanism is governed by ultrafast photothermal demagnetization and coherent spin precession in the subsequent remagnetization process, during which the intrinsic topology and symmetry of the vortex are preserved. Crucially, the helicity switching dynamics can be tuned precisely using the laser fluence and magnetic field strength, enabling deterministic to stochastic control over the two energy-degenerate helicity states. This control was reproduced in micromagnetic simulations when the parameters were optimized within a physically reasonable range.

Magnetization switching is central to the operation of modern spintronic devices, enabling binary information storage and logical operations by encoding information bits '0' and '1' through the alignment of collinear magnetization[1]. However, the manipulation of emergent non-collinear topological spin configurations, such as nanoscale magnetic vortices and skyrmions, has attracted substantial interest as a promising avenue for next-generation information processing technology. This emerging field leverages the unique inherent topological degrees of freedom[2–10], including topological charge, helicity and polarity[11,12], which offer the potential for multistate memory storage[13] via complex spatial topologies[10,14,15], helicity-selective resonances in spin torque oscillators[16] and polarity tunability in magnetic tunnel junctions[17,18]. Topological spin helicity has recently garnered attention due to its promising potential in encoding information[14,19,20], performing neuromorphic[21,22] and probabilistic computing[23,24] and even quantum logic operation[25,26] by manipulating the coherent switching of helicity between the two energy-degenerate states with helicity $\eta = C\pi/2$ in topological spin configurations, where $C = +1$ and $C = -1$ represent the counterclockwise (CCW) and clockwise (CW) swirling directions of the in-plane magnetic moment, respectively.

A full list of affiliations appears at the end of the paper. ✉e-mail: yudp@sustech.edu.cn; houzp@m.scnu.edu.cn; r.dunin-borkowski@fz-juelich.de; zhu@bnl.gov; xwfu@nankai.edu.cn

Helicity switching in topological spin configurations has been intensively explored via electric current[27,28], magnetic[29–33], electric[34] and strain[35] fields. However, these traditional methods usually disrupt the intrinsic topology of the spin configurations during the switching; that is, they break the energy degeneracy of the two helicity states, resulting in incoherent manipulations with long switching times and low controllability. Recently, ultrafast optical excitation has been used for rapid writing/erasing of magnetic skyrmions in the presence of magnetic fields[36,37] and the fast generation of magnetic vortices[38] through the optical quench effect, where the transient temperatures of the systems exceed the Curie temperature (T_C) and the spin relaxation dynamics are incoherent, leading to random helicity of the final vortices[39]. Controllable optical switching of collinear magnetizations has also been realized recently through modifications of the anisotropy field[40–42]. Nevertheless, controllable coherent switching of the helicity in topological spin configurations[43] remains difficult. The challenge lies in achieving globally coherent spin precession while maintaining the intrinsic topology of the spin configurations.

In this article we demonstrate controllable coherent helicity toggle switching between the CCW and CW states of a magnetic vortex by Lorentz electron microscopy imaging, which is driven by a single-shot femtosecond laser pulse with a moderate intensity in the presence of an out-of-plane magnetic field while the transient temperature of the system remains below T_C. Combined dynamical simulations and time-resolved magneto-optical Kerr effect measurements indicate that the coherent helicity switching probably occurs within ~270 ps. The coherent switching behaviour is precisely tunable with respect to the laser fluence and the magnetic field strength. Our results reveal that such non-trivial switching dynamics are governed by ultrafast photothermal demagnetization and coherent spin precession in the subsequent remagnetization process.

Theoretical feasibility of coherent toggle switching of vortex helicity

We first performed a theoretical analysis of the magnetic vortex state in $Ni_{80}Fe_{20}$ permalloy (Py) nanodisks to evaluate the feasibility of achieving coherent helicity toggle switching. Figure 1a illustrates the spin texture of a simulated magnetic vortex state in which the spin transitions continuously from a circular in-plane helicity flux at the periphery to an out-of-plane polarity core at the centre. Considering its circular symmetry, the reduced magnetization $\mathbf{m}$ of the vortex in the disk plane $\mathbf{r}(\chi,\rho)$ can be described by the polar angle $\theta(\chi,\rho)$ and the azimuthal angle $\varphi(\chi,\rho)$ as:

$$m_x + \mathrm{i}m_y = \mathrm{e}^{i\varphi}\sin\theta,\ m_z = \cos\theta \quad (1)$$

$$\varphi(\chi,\rho) = q\chi + C\frac{\pi}{2} \quad (2)$$

where ρ and χ are the radial coordinate and the polar angle of $\mathbf{r}$, respectively, θ determines the polarity $p = \pm 1$ and φ determines the vorticity number q (+1 for a vortex and −1 for an antivortex) and the helicity angle $C\pi/2$ ($C = +1$ for a CCW vortex and $C = -1$ for a CW vortex; Supplementary Video 1). Any arbitrary vortex state $|\psi_C\rangle$ can then be mapped onto a point in the Bloch sphere representation (Fig. 1b):

$$|\psi_C\rangle = \cos\left(\frac{\theta}{2}\right)|0\rangle + \mathrm{e}^{i\varphi}\sin\left(\frac{\theta}{2}\right)|1\rangle \quad (3)$$

where $|0\rangle$ and $|1\rangle$ represent up and down spin polarization states, while $|i+\rangle$ (red) and $|i-\rangle$ (blue) denote CCW and CW vortices, and $|+\rangle$ and $|-\rangle$ correspond to divergent ($C = 0$) and convergent ($C = 2$) spin configurations, respectively (Fig. 1c). Figure 1d shows a projected energy map of the vortex states on the Bloch sphere, which demonstrates that the two energy-degenerate helicity states $|\psi_{\pm1}\rangle$ are separated by a topological energy barrier (E_{tb}) (Fig. 1e). Our calculations show that the maximum value E_{tb1} (in the longitudinal direction) and minimum value E_{tb2} (in the latitudinal direction) are 26.61 and 3.15 keV, respectively, far exceeding the energy scale of gigahertz microwave photons that match the eigenfrequency of vortex excitation. Therefore, traditional pulsed magnetic field and spin current excitations can only drive low-frequency (sub-gigahertz) gyration of the vortex core to achieve polarity or helicity switching in an incoherent manner by disrupting the vortex core[5–7,29,35,44–48].

Ultrafast photothermal demagnetization provides a promising approach for achieving high-frequency spin precession[49,50]. Following femtosecond photoexcitation, the thermalization of electrons results in an immediate reduction in the spontaneous magnetization $M_s(T)$ and a subsequent picosecond spin reorientation that rephases the magnetic orders until the magnetization aligns parallel to the effective field $\mathbf{H}_{eff}$. $\mathbf{H}_{eff}$ is the sum of the external field $\mathbf{H}$ and the shape-anisotropic demagnetization field ($\mathbf{H}_d \approx -4\pi\mathbf{M}$). Both H and M_s are crucial for inducing effective spin precession around the temporally evolving $\mathbf{H}_{eff}$ in the subsequent remagnetization process. This dynamic process is accompanied by lattice heating and follows cooling over periods of hundreds of picoseconds to a few nanoseconds until the system reaches equilibrium, as shown by previous time-resolved Lorentz electron imaging results[51]. We calculated projected energy maps of the vortex states by varying these two parameters (Fig. 1f,g). Our results show that, with increasing H, the two helicity states $|\psi_{\pm1}\rangle$ transform gradually from the barriered $|i\pm\rangle$ states to the unbarriered $|0\rangle$ state along the longitudinal direction (Fig. 1f,h). A decrease in M_s leads to comparable transformations (Fig. 1g,i). In this way, the topological energy barriers E_{tb} can be smoothed temporarily, enabling coherent helicity toggle switching.

Experimental realization of coherent toggle switching of vortex helicity

We observed magnetic vortex variations in a Py disk with a diameter of 1 μm under femtosecond laser pulse excitation (with a fluence of 19.5 mJ cm^{-2}) under different out-of-plane magnetic fields (−300 to 300 mT) using a transmission electron microscope (Fig. 2a and Methods). The CCW and CW vortices exhibit reversed white or black contrast in Fresnel images, allowing the magnetic induction field of a vortex to be reconstructed using the transport of intensity equation (right diagram in Fig. 2a and Methods) and enabling helicity switching behaviours to be distinguished. To ensure reproducibility, we performed 100 repetitions of the femtosecond laser pulse excitation at each magnetic field strength. In zero field, no helicity switching was observed, indicating that the transient spin temperature remained below the T_C of Py (~800 K) (left plot in Fig. 2a and Supplementary Note 1), as otherwise the random appearance of a single-vortex or multiple-vortex state would occur[39]. The spin temperature evolution was further verified by three-temperature model (3TM) calculations (inset in Fig. 2a and Methods)[49,52,53]. With increasing magnetic field, we observed a transition from single-core vortices to multi-core vortices ($C = 0$), followed by reversible switching between $C = +1$ and $C = -1$ vortex states. To illustrate the magnetic-field-dependent switching behaviour, we calculated the absolute values of the helicity difference $|\delta C|$ for the observed switching behaviours by comparing two adjacent vortex states before and after laser pulse excitation under different field strengths. These values were plotted as a greyscale map in Fig. 2b, where the white areas ($|\delta C| = 2$) represent a reversal of the vortex helicity, the grey regions ($|\delta C| = 1$) indicate a transition between single-core and multiple-core vortices, and the black areas ($|\delta C| = 0$) signify no changes in the vortex helicity. The results demonstrate three types of switching behaviours ($|\delta C| = 2, 1, 0$) that vary with the magnetic field.

We further analysed the three types of switching behaviours at specific magnetic fields ($H = 87$, 99 and 131 mT) that correspond to their first appearances (dashed lines in Figs. 2c–e) and present the

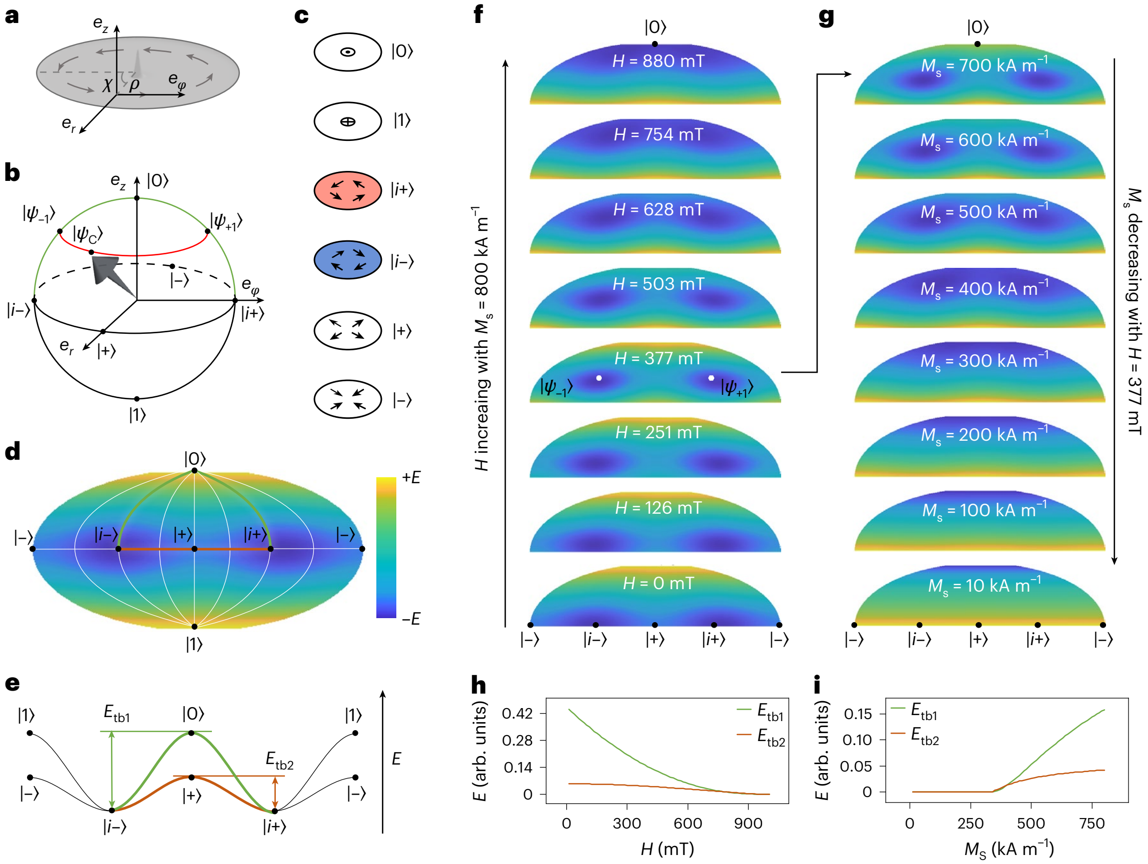

Fig. 1 | Bloch sphere representation of vortex states in a magnetic disk and corresponding energy maps. a, Vortex spin configuration in a confined magnetic disk, represented in cylindrical coordinates (e_r, e_φ, e_z). The reduced magnetization **m** at position **r**(χ, ρ) is indicated by the grey arrows. **b**, Vortex pole states in the Bloch sphere representation. The black arrow indicates the space-averaged magnetization **m**(m_r, m_φ, m_z) corresponding to vortex state $|\psi_C\rangle$ with vortex helicity *C*. The green longitude and red latitude lines denote spin rotations about the e_r and e_z axes. **c**, Schematic representations of the spin configurations of vortex pole states. **d**, Energy map of vortex pole states in zero field. The blue and yellow areas indicate energy minima and maxima, respectively. **e**, Energy levels of vortex pole states in the longitudinal and latitudinal directions of the Bloch sphere. **f**,**g**, Energy evolution as a function of the out-of-plane magnetic field *H* (**f**) and spontaneous magnetization M_s (**g**). The black arrow between **f** and **g** indicates that the M_s-dependent series in **g** is taken at the selected field value *H* = 377 mT from **f**. **h**,**i**, Topological energy barriers plotted as a function of *H* (**h**) and M_s (**i**) (arb. units, arbitrary units).

typical Fresnel images in Fig. 2f–h (Supplementary Note 2). At 87 mT, the vortex helicity switched reversibly between $|\psi_{\pm1}\rangle$ states (Fig. 2f (top) and the left panel of Supplementary Video 2) after each laser pulse excitation, exhibiting a toggle switching characteristic with a switching probability that approached 100% (Fig. 2f (bottom). At 99 mT, the three types of switching behaviour occurred stochastically, with the probabilities of helicity switching and non-switching approaching ~40% and the probability of multi-core vortices being ~20% (Fig. 2g (bottom), Supplementary Fig. 3 and the middle panel of Supplementary Video 2). A further increase in *H* to 131 mT, however, resulted in no helicity switching (Fig. 2h (bottom) and right panel of Supplementary Video 2). This alternative transformation indicates the high magnetic-field tunability of the laser-induced helicity switching. Moreover, the independence of both laser polarization and field direction exclude a possible dominant contribution from the inverse Faraday effect[54] or inverse Cotton–Mouton effect[55], suggesting that photothermal demagnetization plays a crucial role.

Dynamical model of helicity switching processes

To understand the underlying mechanism, we simulated the spatiotemporal evolution of the vortex states $|\psi_C\rangle$ by incorporating 3TM scaling with photothermal demagnetization into the Landau–Lifshitz–Gilbert equation (Methods and Supplementary Note 1). As shown in the left panel of Fig. 3a, the initial direction of **M** (for example, CW vortex state $|\psi_{-1}\rangle$, indicated by the blue arrow) is taken along the direction of $\mathbf{H}_{\mathrm{eff}}$ (indicated by the blue dashed line). During demagnetization, the rapid decrease in spontaneous magnetization ($M_s(t)/M_s$ = 3.5% at 19.5 mJ cm^{-2}) results in a sudden drop in $\mathbf{H}_{\mathrm{d}}$ and thus a reorientation of $\mathbf{H}_{\mathrm{eff}}$ (light blue dashed line in the right panel of Fig. 3a). As the demagnetization process (on femtosecond timescales) is much faster than the spin precession period (tens to hundreds of picoseconds), **M** is unable to follow $\mathbf{H}_{\mathrm{eff}}$ and begins to precess around the temporally evolving $\mathbf{H}_{\mathrm{eff}}$ with an angular velocity of $\omega = \gamma H_{\mathrm{eff}}$ (right panel of Fig. 3a), where γ is the gyromagnetic ratio. In the subsequent remagnetization, $\mathbf{H}_{\mathrm{eff}}$ evolves with the **M** precessing around it until the system reaches equilibrium (red arrows in the right panel of Fig. 3a).

Using this model, our numerical simulations reproduced the three observed types of helicity switching behaviour with increasing magnetic field, as illustrated by the colour transformations between blue (CW vortex state $|\psi_{-1}\rangle$) and red (CCW vortex state $|\psi_{+1}\rangle$) regions in Fig. 3b. To obtain deeper insight into the microscopic dynamics of the three types of helicity switching behaviour ($|\delta C|$ = 2, 1 and 0), we analysed their spatiotemporal spin helicity evolution and trajectories of the vortex states on the projected energy map of the Bloch sphere (Fig. 3c–e). At 88 mT, following demagnetization the initial CW vortex state located at the left energy minimum point $|\psi_{-1}\rangle$ of the Bloch sphere shifts to the |0⟩ state, initiating a right-handed helix rotation of the vortex state (white trace in the right panel of Fig. 3c) towards a new energy minimum point (0–0.05 ns, right panel of Fig. 3c). During the subsequent remagnetization (0.05–0.80 ns), the energy minimum point gradually

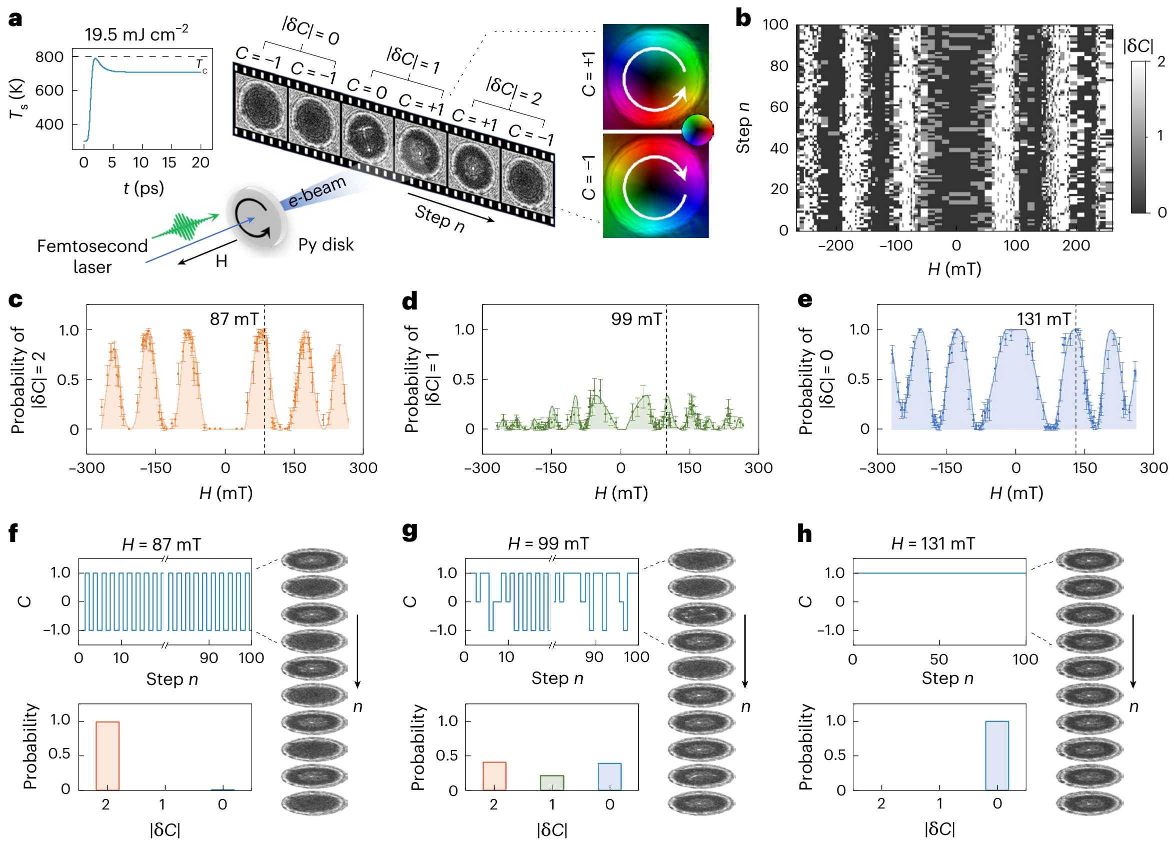

Fig. 2 | Magnetic-field-dependent vortex helicity switching under single-shot femtosecond laser pulse excitation. a, Left: calculated time evolution of the spin temperature T_s below T_C with an excitation laser fluence of 19.5 mJ cm^{-2}. Centre: Fresnel images showing white-core ($C = +1$), black-core ($C = -1$) and multi-core vortices ($C = 0$). Right: reconstructed magnetic induction maps of CCW ($C = +1$) and CW ($C = -1$) vortex spin configurations. The inset shows a schematic diagram of Lorentz imaging of a magnetic vortex in a Py disk during in situ femtosecond laser excitation in a custom-built transmission electron microscope. **b**, Helicity switching behaviours of vortex states $|\delta C|$ in varying magnetic fields over 100 successive laser pulse excitations. **c**–**e**, Probabilities of three field-dependent helicity switching behaviours: $|\delta C| = 2$ (**c**), $|\delta C| = 1$ (**d**) and $|\delta C| = 0$ (**e**). Data are presented as the probabilities of different types of helicity switching (dots) and the dashed lines indicate the typical behaviours. The error bars represent two-sided 95% confidence intervals estimated using the normal approximation to the binomial distribution. Each data point was obtained from 100 repeated single-shot femtosecond laser excitations ($n = 100$) applied to the magnetic vortex. The solid line serves as a guideline, with the shaded area indicating the region it encloses. **f**–**h**, Top: vortex helicities over 100 repetitive laser pulse excitation steps n for three magnetic field strengths: 87 mT (**f**), 99 mT (**g**) and 131 mT (**h**). Bottom: corresponding probability distributions of the helicity switching for different $|\delta C|$ states. Right: representative Fresnel images.

splits into two energy-degenerate points ($|\psi_{-1}\rangle$ and $|\psi_{+1}\rangle$), which both shift downwards along the longitudinal direction, eventually crossing and trapping the trajectory at another energy minimum point $|\psi_{+1}\rangle$ at ~0.2 ns. At this point, vortex helicity switching occurs, determining the final helicity of the vortex state in the following relaxation process (left panel of Fig. 3c). The temporal evolutions of the space-averaged magnetization components $\mathbf{m}(m_r, m_\varphi, m_z)$ always remain in phase, with little change in the modulus $|\mathbf{m}|$ (Fig. 3f and Supplementary Fig. 4a). This indicates coherent spin precession during the helicity switching (Supplementary Fig. 4a and left panel of Supplementary Video 3), which means that all of the spins undergo synchronized precession around their time-evolving $\mathbf{H}_{\mathrm{eff}}$.

For the random helicity switching at 100 mT (Fig. 3d), the rotation of the vortex state on the Bloch sphere (white trace in Fig. 3d and Supplementary Fig. 4b) accelerates due to the increased ω, preventing its trajectory from being trapped by the energy minimum point $|\psi_{+1}\rangle$ during remagnetization (0.05–0.80 ns). Instead, the faster rotation drives the vortex state to a TCP at ~0.80 ns (right panel of Fig. 3d), the saddle point between the two split energy minimum points. At this point, the system exhibits a divergent spin configuration and the coherence of the dynamics is disrupted (Fig. 3g and Supplementary Fig. 4b). In the subsequent remagnetization, numerous vortex–antivortex defects emerge, dance and annihilate at the edge, resulting in a final spin configuration that settles randomly into a CW vortex, a CCW vortex or multi-vortex states (middle panel of Supplementary Video 3). At a higher field of 126 mT, the faster rotation of the vortex state (white trace in Fig. 3e and Supplementary Fig. 4c) allows it to bypass the TCP. The trajectory encircles the Bloch sphere and is recaptured by the CW energy minimum point $|\psi_{-1}\rangle$ at ~0.4 ns, with the helicity returning (Fig. 3e and right panel of Supplementary Video 3) in a coherent manner (Fig. 3h and Supplementary Fig. 4c). A criterion for identifying topological critical fluctuations during the energy evolution of vortex states on the Bloch sphere can therefore be established, and can be scaled by $|\mathbf{m}|$ and its partial component m_φ (Fig. 3i). The coherent nature and picosecond timescale of the coherent helicity non-switching in Fig. 3e were further confirmed by measurements of the time-resolved magneto-optical Kerr effect, which suggest that the helicity probably finishes the switching process within ~270 ps (Supplementary Fig. 5, Supplementary Note 4 and Methods).

Laser-fluence-dependent vortex helicity switching behaviour

We performed measurements on vortices at two lower laser fluences (17.7 and 15.0 mJ cm^{-2}). Similar to values obtained under the high fluence (19.5 mJ cm^{-2}; top panel of Fig. 4a), the values of $\langle|\delta C|\rangle$ also exhibit alternating peaks with increasing H (middle and bottom plots in Fig. 4a and

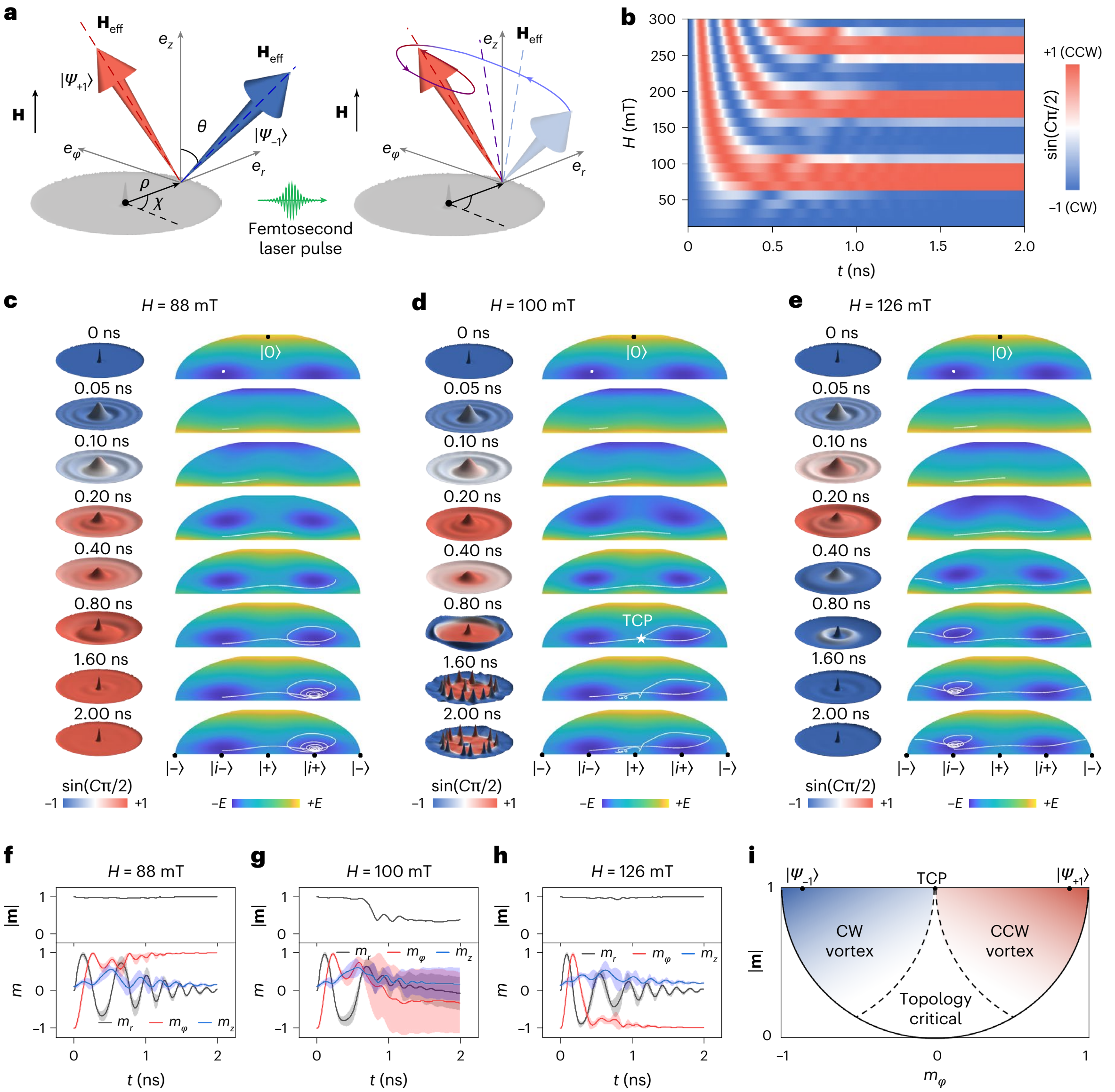

Fig. 3 | Dynamical model and micromagnetic simulations of field-dependent vortex helicity switching. a, Schematic diagrams of laser-induced vortex helicity switching under an out-of-plane magnetic field. Left: ground state ($|\psi_{+1}\rangle$ or $|\psi_{-1}\rangle$), with red and blue arrows corresponding to a CCW vortex $|\psi_{+1}\rangle$ and a CW vortex $|\psi_{-1}\rangle$, respectively. The dashed lines indicate $\mathbf{H}_{\text{eff}}$. Right: laser-excited state, with the coloured curve showing spin precession around $\mathbf{H}_{\text{eff}}$ from $|\psi_{-1}\rangle$ to $|\psi_{+1}\rangle$. **b**, Simulated time evolution of C under varying magnetic fields with a fluence of 19.5 mJ cm^{-2}. For $H < 60$ mT, there is no helicity switching ($|\delta C| = 0$). For H between 60 and 88 mT, helicity reversal ($|\delta C| = 2$) occurs at 170–300 ps, resulting in the final CCW state. For H between 100 and 110 mT, the single-core vortex changes to multi-core vortices ($|\delta C| = 1$). For H between 113 and 138 mT, the CW helicity first reverses to CCW at 105–130 ps and then returns to CW at 300–480 ps, ultimately relaxing to the initial CW state ($|\delta C| = 0$). When H increases further, the three types of helicity switching occur alternately, depending on the number of intermediate reversals. **c**–**e**, Representative helicity switching processes under typical magnetic fields of $H = 88$ mT (**c**), 100 mT (**d**) and 126 mT (**e**) with a fluence of 19.5 mJ cm^{-2}. Left: snapshots of the vortex helicity (blue/red) and m_z (height) distributions during switching. Right: temporal evolution of the projected energy maps in a Bloch sphere representation, with the corresponding trajectories (white traces) of the vortex states shown on the left. Blue and yellow correspond to energy minima and maxima, respectively. The white star in **d** marks the topological critical point (TCP), at which phase diffusion occurs. **f**–**h**, Time evolution of the space-averaged magnetization $\mathbf{m}(m_r, m_\varphi, m_z)$ under magnetic fields of $H = 88$ mT (**f**), 100 mT (**g**) and 126 mT (**h**). The error bars represent the standard deviation of the spatially averaged magnetization components calculated over all discretized simulation cells within the disk. **i**, Schematic diagram of topological critical behaviour during vortex helicity switching. The TCP signifies dephasing of the vortex state, which drops into the inner space of the Bloch sphere, accompanied by dramatic topological critical fluctuations and the random formation of topological defects.

Supplementary Fig. 6). The critical magnetic fields (the peak positions of $\langle|\delta C|\rangle = 2$) for coherent helicity switching shift to higher values as the fluence decreased (red arrow in Fig. 4a). To understand this behaviour, we performed numerical simulations of the phase diagram of $|\delta C|$ values for laser fluences ranging from 14.5 to 19.5 mJ cm^{-2} (Fig. 4b and Supplementary Note 6), which closely reproduced the experimental results (Fig. 4a). Thus, the helicity switching behaviour can also be tuned by adjusting the laser fluence without changing the magnetic field and the final helicity of the vortex state is determined by the number l of intermediate helicity reversals. For example, at 163 mT, the helicity reverses once ($l = 1$) at 14.5 mJ cm^{-2}, resulting in coherent helicity switching (J_1 in Fig. 4b and left panel of Supplementary Video 4). It reverses twice ($l = 2$) and three times ($l = 3$) at 16.3 and 19.5 mJ cm^{-2}, leading to coherent helicity non-switching (J_2 in Fig. 4b and the middle panel of Supplementary Video 4) and coherent helicity switching (J_3 in Fig. 4b and the right panel of Supplementary Video 4), respectively.

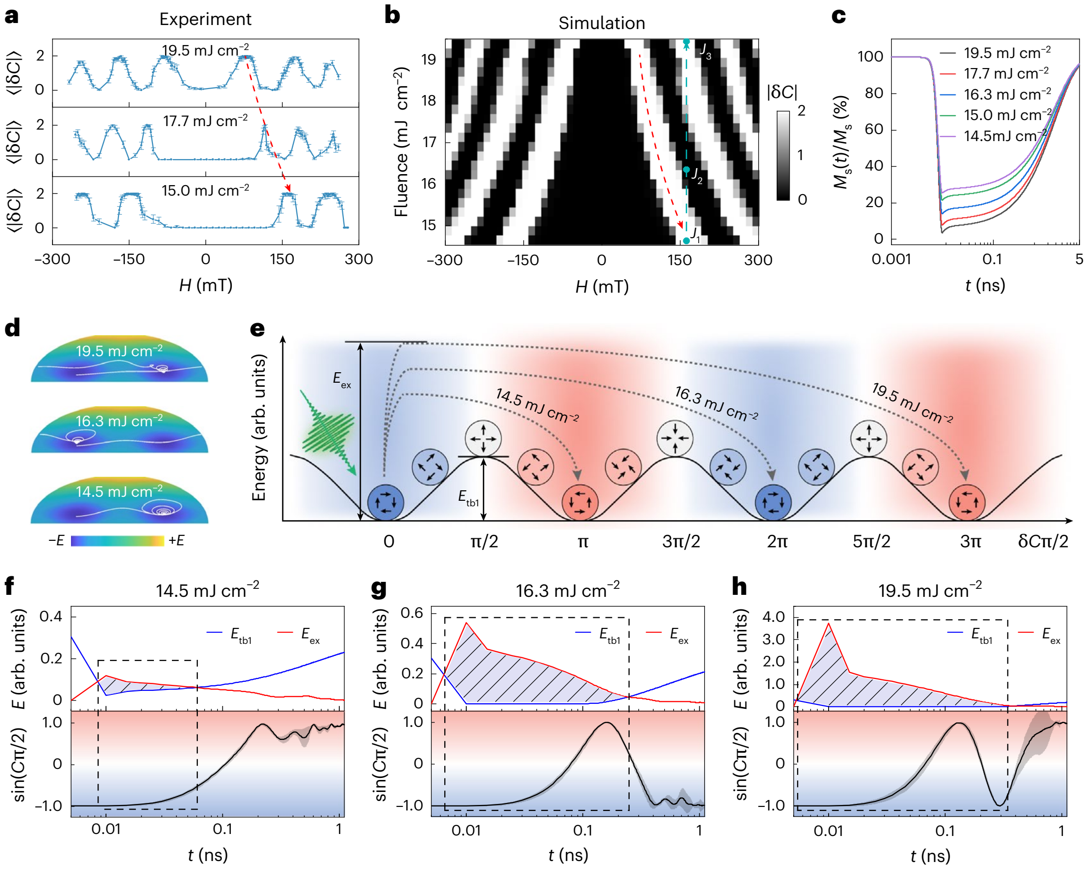

Fig. 4 | Laser-fluence-dependent vortex helicity switching behaviour. **a**, Experimental observations of laser-fluence-dependent vortex helicity switching behaviour. The blue line indicates the expected values of ⟨|δC|⟩ under fluences of 19.5, 17.7 and 15.0 mJ cm^{-2} (top to bottom). The red dashed arrow indicates a shift in the magnetic field required for helicity switching with decreasing laser fluence.The error bars indicate two-sided 95% confidence intervals, estimated using the normal approximation to the binomial distribution. **b**, Simulated vortex helicity switching behaviour (|δC|) as a function of laser fluence and magnetic field strength. The coherent toggle switching behaviours (|δC| = 2, represented by alternating white regions) shift continuously to higher *H* with decreasing laser fluence. The red dashed arrow indicates a magnetic field shift for helicity switching compared with that in **a**. The cyan dashed arrow indicates laser-fluence-tuned helicity reversal once (J_1 = 14.5 mJ cm^{-2}), twice (J_2 = 16.3 mJ cm^{-2}) and three times (J_3 = 19.5 mJ cm^{-2}) under a fixed magnetic field (*H* = 163 mT). **c**, Calculated photothermal demagnetization curves $M_s(t)/M_s$ for laser fluences of between 14.5 and 19.5 mJ cm^{-2}. **d**, Representative trajectories of vortex states (white traces, 0–2.00 ns) on a projected energy map of the Bloch sphere, showing changes in helicity angle δCπ/2 of π, 2π and 3π for fluences J_1, J_2 and J_3. **e**, Energy evolution of the vortex state with changes in helicity angle δCπ/2, illustrating the energy crossover between E_{ex} of the vortex state and E_{tb1}. **f**–**h**, Calculated energy crossover ($E_{tb1} < E_{ex}$) within the time window (dashed box) that permits helicity switching for laser fluences of 14.5 (**f**), 16.3 (**g**) and 19.5 mJ cm^{-2} (**h**) at *H* = 163 mT. Top: calculated time-dependent E_{ex} of the vortex state and E_{tb1}. The hatched shaded areas indicate the energy crossover region ($E_{tb1} < E_{ex}$). Bottom: corresponding time evolution of vortex helicity after laser pulse excitation. The error bars represent the standard deviation of the spatially averaged magnetization components calculated over all discretized simulation cells within the disk, indicated by the grey envelopes. The coloured shading areas represent different helicity regions, with blue indicating CW helicity and red indicating CCW helicity.

This laser-fluence dependence is dominated by the demagnetization process that reshapes the time evolution of the projected energy map of the vortex state on the Bloch sphere. The 3TM calculations indicate that the transient minimum spontaneous magnetization ($M_s(t)/M_s$) on photoexcitation ranges from 25% to 3.5% as the fluence increases from 14.5 to 19.5 mJ cm^{-2} (Fig. 4c and Methods). The corresponding vortex state trajectories with helicity angles rotated by π, 2π and 3π for photoexcitation at J_1 (14.5 mJ cm^{-2}), J_2 (16.3 mJ cm^{-2}) and J_3 (19.5 mJ cm^{-2}) at *H* = 163 mT (Fig. 4b) are plotted in Fig. 4d (Supplementary Note 7). The rotation processes can be schematically illustrated by comparing the energy evolution of the excited vortex state with the changes in its helicity angle (Fig. 4e and Supplementary Note 8). Following demagnetization, the transiently excited energy E_{ex} of the initial CW vortex state increases with the laser fluence and exceeds E_{tb1}, initiating a right-handed helix rotation of the vortex state on the Bloch sphere with increasing the helicity angle. During remagnetization, the helix rotation with higher E_{ex} overcomes E_{tb1} at larger fractional changes of the helicity angle (δCπ/2 = π/2, 3π/2 or 5π/2). As the damping effect drives E_{ex} to below E_{tb1}, it finally converges at an energy minimum point with an integer change in the helicity angle (δCπ/2 = π, 2π or 3π) for the ultimate vortex state.

To verify the energy evolution during the helix rotation, we calculated the time-dependent E_{ex} and E_{tb1} for different excitation fluences (J_1 to J_3) at 163 mT (Fig. 4f–h). For the single helicity reversal at J_1, ultrafast demagnetization ($M_s(t)/M_s$ = 25%) results in an energy crossover ($E_{tb1} < E_{ex}$) within a time window of ~50 ps, which reduces E_{tb1} temporarily to 0.02 and raises E_{ex} to 0.12 (dashed areas in the top panel of Fig. 4f). Before E_{tb1} recovers to an energy level higher than E_{ex} at ~55 ps, the trajectory of the vortex state overcomes E_{tb} with a π/2-rotated helicity angle and is trapped by another energy minimum point ($|\psi_{+1}\rangle$), completing the coherent helicity switching (bottom panel of Fig. 4f and Supplementary Notes 7 and 8). For the two helicity reversals at J_2, photothermal demagnetization ($M_s(t)/M_s$ = 14%) reduces E_{tb1} sufficiently and excites E_{ex} to 0.54, where the energy crossover ($E_{tb1} < E_{ex}$) persists for a time window of ~230 ps and allows the trajectory of the vortex state to approach a 3π/2-rotated helicity angle, leading to coherent helicity non-switching

(Fig. 4g and Supplementary Notes 7 and 8). At the higher fluence of J_3, greater photothermal demagnetization ($M_s(t)/M_s = 3.5\%$) results in a longer time window (~375 ps) for the energy crossover ($E_{tb1} < E_{ex}$), which allows three vortex helicity reversals, resulting in a final vortex state with a switched helicity (Fig. 4h and Supplementary Notes 7 and 8).

Conclusions

In conclusion, we demonstrate picosecond-scale coherent toggle switching of the topological spin helicity in symmetric Py disks with high robustness and tunability with out-of-plane-magnetic-field-assisted femtosecond laser pulse excitation. The coherent helicity toggle switching occurs when either the magnetic field or the laser fluence are increased. Theoretical simulations reveal that the switching mechanism is based on transient reshaping of the projected energy landscape on the Bloch sphere induced by photothermal demagnetization, which drives the vortex state to undergo coherent magnetization precession in the subsequent remagnetization. This mechanism should be applicable to other topological swirling spin textures, such as Bloch-type skyrmions with energy-degenerate helicity states. It has been theoretically proposed that coherently controllable helicity switching of topological swirling spin configurations has the potential to mimic qubit operation by encoding the superposition state ($|\psi_C\rangle$) of the two energy-degenerate CW ($|i-\rangle$) and CCW ($|i+\rangle$) helicity states on the Bloch sphere[25,26,56]. Our findings may provide a route to these applications at room temperature (Supplementary Note 9).

Online content

Any methods, additional references, Nature Portfolio reporting summaries, source data, extended data, supplementary information, acknowledgements, peer review information; details of author contributions and competing interests; and statements of data and code availability are available at https://doi.org/10.1038/s41565-026-02142-z.

References

1. Fert, A. et al. Electrical control of magnetism by electric field and current-induced torques. *Rev. Mod. Phys.* **96**, 015005 (2024).
2. Shinjo, T. et al. Magnetic vortex core observation in circular dots of permalloy. *Science* **289**, 930–932 (2000).
3. Wachowiak, A. et al. Direct observation of internal spin structure of magnetic vortex cores. *Science* **298**, 577–580 (2002).
4. Pribiag, V. S. et al. Magnetic vortex oscillator driven by d.c. spin-polarized current. *Nat. Phys.* **3**, 498–503 (2007).
5. Yamada, K. et al. Electrical switching of the vortex core in a magnetic disk. *Nat. Mater.* **6**, 270–273 (2007).
6. Uhlíř, V. et al. Dynamic switching of the spin circulation in tapered magnetic nanodisks. *Nat. Nanotechnol.* **8**, 341–346 (2013).
7. Van Waeyenberge, B. et al. Magnetic vortex core reversal by excitation with short bursts of an alternating field. *Nature* **444**, 461–464 (2006).
8. Pigeau, B. et al. Optimal control of vortex-core polarity by resonant microwave pulses. *Nat. Phys.* **7**, 26–31 (2011).
9. Yu, X. et al. Magnetic stripes and skyrmions with helicity reversals. *Proc. Natl Acad. Sci. USA* **109**, 8856–8860 (2012).
10. Tang, J. et al. Magnetic skyrmion bundles and their current-driven dynamics. *Nat. Nanotechnol.* **16**, 1086–1091 (2021).
11. Wild, J. et al. Entropy-limited topological protection of skyrmions. *Sci. Adv.* **3**, e1701704 (2017).
12. Suess, D. et al. Topologically protected vortex structures for low-noise magnetic sensors with high linear range. *Nat. Electron.* **1**, 362–370 (2018).
13. Bohlens, S. et al. Current controlled random-access memory based on magnetic vortex handedness. *Appl. Phys. Lett.* **93**, 142508 (2008).
14. Wang, Y. et al. Electric-field-driven non-volatile multi-state switching of individual skyrmions in a multiferroic heterostructure. *Nat. Commun.* **11**, 3577 (2020).
15. Zheng, F. et al. Hopfion rings in a cubic chiral magnet. *Nature* **623**, 718–723 (2023).
16. Hu, C. et al. Auto-oscillations for the coupling between breathing mode and chiral switching in magnetic skyrmions. *J. Phys. D* **54**, 015005 (2021).
17. Li, S. et al. Experimental demonstration of skyrmionic magnetic tunnel junction at room temperature. *Sci. Bull.* **67**, 691–699 (2022).
18. Chen, S. et al. All-electrical skyrmionic magnetic tunnel junction. *Nature* **627**, 522–527 (2024).
19. Geng, L. D. & Jin, Y. M. Magnetic vortex racetrack memory. *J. Magn. Magn. Mater.* **423**, 84–89 (2017).
20. Koraltan, S. et al. Generation and annihilation of skyrmions and antiskyrmions in magnetic heterostructures. *Phys. Rev. B* **108**, 134401 (2023).
21. Song, K. M. et al. Skyrmion-based artificial synapses for neuromorphic computing. *Nat. Electron.* **3**, 148–155 (2020).
22. Yokouchi, T. et al. Pattern recognition with neuromorphic computing using magnetic field–induced dynamics of skyrmions. *Sci. Adv.* **8**, eabq5652 (2022).
23. Puttock, R. et al. Stochastic hexagonal injectors in artificial spin ice. *Commun. Mater.* **5**, 207 (2024).
24. Borders, W. A. et al. Integer factorization using stochastic magnetic tunnel junctions. *Nature* **573**, 390–393 (2019).
25. Psaroudaki, C. & Panagopoulos, C. Skyrmion qubits: a new class of quantum logic elements based on nanoscale magnetization. *Phys. Rev. Lett.* **127**, 067201 (2021).
26. Xia, J. et al. Universal quantum computation based on nanoscale skyrmion helicity qubits in frustrated magnets. *Phys. Rev. Lett.* **130**, 106701 (2023).
27. Lim, W. L. et al. Fast chirality reversal of the magnetic vortex by electric current. *Appl. Phys. Lett.* **105**, 222405 (2014).
28. Yakata, S. et al. Chirality control of magnetic vortex in a square Py dot using current-induced Oersted field. *Appl. Phys. Lett.* **99**, 242507 (2011).
29. Jaafar, M. et al. Control of the chirality and polarity of magnetic vortices in triangular nanodots. *Phys. Rev. B* **81**, 054439 (2010).
30. Gaididei, Y., Sheka, D. D. & Mertens, F. G. Controllable switching of vortex chirality in magnetic nanodisks by a field pulse. *Appl. Phys. Lett.* **92**, 012503 (2008).
31. Antos, R. & Otani, Y. Simulations of the dynamic switching of vortex chirality in magnetic nanodisks by a uniform field pulse. *Phys. Rev. B* **80**, 140404 (2009).
32. Konoto, M. et al. Formation and control of magnetic vortex chirality in patterned micromagnet arrays. *J. Appl. Phys.* **103**, 023904 (2008).
33. Xie, K. et al. Determination of magnetic vortex chirality by local field excited gyration. *Appl. Phys. Lett.* **105**, 102402 (2014).
34. Yao, X., Chen, J. & Dong, S. Controlling the helicity of magnetic skyrmions by electrical field in frustrated magnets. *New J. Phys.* **22**, 083032 (2020).
35. Zhang, Y. et al. Deterministic reversal of single magnetic vortex circulation by an electric field. *Sci. Bull.* **65**, 1260–1267 (2020).
36. Berruto, G. et al. Laser-induced skyrmion writing and erasing in an ultrafast cryo-Lorentz transmission electron microscope. *Phys. Rev. Lett.* **120**, 117201 (2018).
37. Li, Z. et al. Room-temperature sub-100 nm Néel-type skyrmions in non-stoichiometric van der Waals ferromagnet $Fe_{3-x}GaTe_2$ with ultrafast laser writability. *Nat. Commun.* **15**, 1017 (2024).
38. Eggebrecht, T. et al. Light-induced metastable magnetic texture uncovered by in situ Lorentz microscopy. *Phys. Rev. Lett.* **118**, 097203 (2017).

39. Fu, X. et al. Optical manipulation of magnetic vortices visualized in situ by Lorentz electron microscopy. *Sci. Adv.* **4**, eaat3077 (2018).
40. Davies, C. S. et al. Anomalously damped heat-assisted route for precessional magnetization reversal in an iron garnet. *Phys. Rev. Lett.* **122**, 027202 (2019).
41. Peng, Y. et al. In-plane reorientation induced single laser pulse magnetization reversal. *Nat. Commun.* **14**, 5000 (2023).
42. Zalewski, T. et al. Ultrafast all-optical toggle writing of magnetic bits without relying on heat. *Nat. Commun.* **15**, 4451 (2024).
43. Yu, D. et al. Skyrmions-based logic gates in one single nanotrack completely reconstructed via chirality barrier. *Natl Sci. Rev.* **9**, nwac021 (2022).
44. Im, M.-Y. et al. Symmetry breaking in the formation of magnetic vortex states in a permalloy nanodisk. *Nat. Commun.* **3**, 983 (2012).
45. Schneider, M. et al. Stability of magnetic vortices in flat submicron permalloy cylinders. *J. Appl. Phys.* **92**, 1466–1472 (2002).
46. Lau, J. W., Beleggia, M. & Zhu, Y. Common reversal mechanisms and correlation between transient domain states and field sweep rate in patterned permalloy structures. *J. Appl. Phys.* **102**, 043906 (2007).
47. Kammerer, M. et al. Magnetic vortex core reversal by excitation of spin waves. *Nat. Commun.* **2**, 279 (2011).
48. Schneider, M., Hoffmann, H. & Zweck, J. Magnetic switching of single vortex permalloy elements. *Appl. Phys. Lett.* **79**, 3113–3115 (2001).
49. Beaurepaire, E. et al. Ultrafast spin dynamics in ferromagnetic nickel. *Phys. Rev. Lett.* **76**, 4250–4253 (1996).
50. Kirilyuk, A., Kimel, A. V. & Rasing, T. Ultrafast optical manipulation of magnetic order. *Rev. Mod. Phys.* **82**, 2731–2784 (2010).
51. Rubiano da Silva, N. et al. Nanoscale mapping of ultrafast magnetization dynamics with femtosecond Lorentz microscopy. *Phys. Rev. X* **8**, 031052 (2018).
52. Koopmans, B. et al. Explaining the paradoxical diversity of ultrafast laser-induced demagnetization. *Nat. Mater.* **9**, 259–265 (2010).
53. Kim, J.-W. et al. Ultrafast spin demagnetization by nonthermal electrons of TbFe alloy film. *Appl. Phys. Lett.* **94**, 192506 (2009).
54. Taguchi, K., Ohe, J. -i & Tatara, G. Ultrafast magnetic vortex core switching driven by the topological inverse Faraday effect. *Phys. Rev. Lett.* **109**, 127204 (2012).
55. Shen, L. Q. et al. Dominant role of inverse Cotton-Mouton effect in ultrafast stimulation of magnetization precession in undoped yttrium iron garnet films by 400-nm laser pulses. *Phys. Rev. B* **97**, 224430 (2018).
56. Pan, X.-F. et al. Skyrmion-mechanical hybrid quantum systems: manipulation of skyrmion qubits via phonons. *Phys. Rev. Res.* **6**, 023067 (2024).

---

[1]Ultrafast Electron Microscopy Laboratory, The MOE Key Laboratory of Weak-Light Nonlinear Photonics, School of Physics, Nankai University, Tianjin, China. [2]Guangdong Provincial Key Laboratory of Optical Information Materials and Technology, Institute for Advanced Materials, South China Academy of Advanced Optoelectronics, South China Normal University, Guangzhou, China. [3]Beijing National Laboratory for Condensed Matter Physics, Institute of Physics, Chinese Academy of Sciences, Beijing, China. [4]Songshan Lake Materials Laboratory, Dongguan, China. [5]Research Institute of Interdisciplinary Science and School of Materials Science and Engineering, Dongguan University of Technology, Dongguan, China. [6]Ernst Ruska-Centre for Microscopy and Spectroscopy with Electrons and Peter Grunberg Institute, Forschungszentrum Jülich, Jülich, Germany. [7]Tianjin Key Lab for Rare Earth Materials and Applications, Smart Sensor Interdisciplinary Science Center, School of Materials Science and Engineering, Nankai University, Tianjin, China. [8]State Key Laboratory for Mesoscopic Physics and Frontiers Science Center for Nano-optoelectronics, School of Physics, Peking University, Beijing, China. [9]Laboratory of Solid State Microstructures and Innovation Center of Advanced Microstructures, Nanjing University, Nanjing, China. [10]International Quantum Academy, Shenzhen, China. [11]Condensed Matter Physics and Materials Science Department, Brookhaven National Laboratory, Upton, NY, USA. [12]Academy for Advanced Interdisciplinary Studies, Nankai University, Tianjin, China. [13]School of Materials Science and Engineering, Smart Sensing Interdisciplinary Science Center, Nankai University, Tianjin, China. [14]These authors contributed equally: Can Liu, Zefang Li, Xuange Hu.
✉e-mail: yudp@sustech.edu.cn; houzp@m.scnu.edu.cn; r.dunin-borkowski@fz-juelich.de; zhu@bnl.gov; xwfu@nankai.edu.cn

Methods

Projected energy map of the vortex state on the Bloch sphere

The point $|\psi_C\rangle$ of the vortex state on the Bloch sphere is defined by θ and φ in cylindrical coordinates (e_r, e_φ, e_z) with rotational symmetry. To calculate the projected energy map of the vortex state on the Bloch sphere, we relaxed the field-polarized vortex states $|\psi_\pm\rangle$ from $|i\pm\rangle$ to $|\pm\rangle$ along the longitudinal direction and then continuously rotated the helicity angle to obtain arbitrary $|\psi_C\rangle$ vortex states along the latitudinal direction. The coordinates of the energy map were transformed using a Mollweide projection. The colour scale represents the free energy, which is normalized by dividing by $\mu_0 M_s^2 V_0$, where V_0 is the volume of the mesh size.

In situ Lorentz imaging of magnetic vortices in Py disks

Symmetric Py disks (30 nm thick and 1 μm in diameter) were prepared by magnetron sputtering onto a Si_3N_4 membrane (50 nm thick with a 500 μm × 500 μm window area on a Si frame) with pre-patterned symmetric circles using electron-beam lithography followed by a lift-off process. Lorentz imaging of vortices in a symmetric Py disk was carried out in a custom-built transmission electron microscope (FEI Talos F200i) using an overfocus imaging mode (d = +3 mm) with a continuous electron beam at 200 kV. Magnetic induction maps of CCW and CW vortex spin configurations were obtained using the transport of intensity equation, and two defocused Lorentz images (±1.5 mm) were used for the reconstruction. Linearly polarized single-shot femtosecond laser pulses (515 nm wavelength, ~120 μm spot size, 300 fs pulse duration) were generated by using a combination of an infrared femtosecond laser source (1,030 nm wavelength, Spirit 1030-100 manufactured by Spectra-Physics), second-harmonic generation (nonlinear crystal β-BaB_2O_4 to produce 515 nm laser pulses) and a digital delay generator (Stanford research system DG645) for an external trigger of the femtosecond laser source at a frequency of 0.5 Hz. The resulting 2 s interval between successive laser pulses ensured that the magnetic vortex reached thermal equilibrium after each step of laser pulse excitation. For each laser fluence and magnetic field, more than 100 Lorentz images were captured to record occurrences of white cores (C = +1), black cores (C = −1) and multi-core vortices (C = 0). The probabilities and confidence intervals of the three types of switching behaviour ($|\delta C| = 2, 1, 0$) were calculated using a binomial distribution. The parameters used to calculate the laser fluence are listed in Supplementary Note 10.

Time-resolved magneto-optical Kerr effect measurements on magnetic vortices in Py disks

The time-resolved magneto-optical Kerr effect measurements were performed using a two-colour femtosecond laser system (Supplementary Fig. 5a). Both the pump (700 nm) and probe (1,030 nm) pulses were derived from a common femtosecond laser source (Spirit-100, Spectra-Physics) operating at a repetition rate of 100 kHz. The fundamental 1,030 nm femtosecond pulses with a pulse duration of ~300 fs served directly as the probe. The 700 nm femtosecond pump pulses with a pulse duration of ~30 fs were generated using a non-collinear optical parametric amplifier (Spirit-NOPA 2H, Spectra-Physics). These two laser beams were focused onto the sample at a normal incidence configuration through a ×50 objective lens (LMPLFLN50X, Olympus), yielding a spot size of ~2 μm in diameter. The reflected probe beam was then guided to pass a filter that blocks the reflection of pump, then a half-wave plate and a Wollaston prism before being collected by a balanced detector (PDB220A2/M, Thorlabs). A lock-in amplifier (MFLI 5 MHz, Zurich Instruments) was used to process data with high signal-to-noise ratios. The time delay between the pump and probe pulses was controlled by a mechanical translation stage (DDS600-E, Thorlabs). The sample was mounted in the chamber of a magnet optical cryostat (OptiCool, Quantum Design), and an external magnetic field of ~130 mT was applied perpendicular to the sample plane, parallel to the incident laser beam. The fluences of the probe and pump beams were set to ~1.4 mJ cm^{-2} and ~19.5 mJ cm^{-2}, respectively.

Laser-induced dynamical micromagnetic simulations

Based on the finite difference method and a Runge–Kutta solver with adaptive time-step control[57], we developed a laser-induced dynamical micromagnetic simulation code by incorporating a 3TM scaling with photothermal demagnetization into the Landau–Lifshitz–Gilbert equation:

$$\frac{\mathrm{d}\mathbf{m}}{\mathrm{d}t} = -\frac{\gamma}{1+\alpha^2}\left(\mathbf{m}\times\mathbf{h}_{\mathrm{eff}}\right) - \frac{\alpha\gamma}{1+\alpha^2}\left[\mathbf{m}\times\left(\mathbf{m}\times\mathbf{h}_{\mathrm{eff}}\right)\right] \tag{4}$$

where $\mathbf{m} = \mathbf{M}/M_s$ represents the reduced magnetization, t is time in units of $(\gamma M_s)^{-1}$, α is the Gilbert damping coefficient and $\mathbf{h}_{\mathrm{eff}} = \mathbf{H}_{\mathrm{eff}}/M_s$ is the normalized effective field obtained by taking the variational derivative $-\delta\varepsilon/\delta m$ of the normalized free energy:

$$\varepsilon = -\int\left[\frac{A}{\mu_0 M_s^2}(\nabla\mathbf{m})^2 - \frac{1}{2}\mathbf{m}\cdot\mathbf{h}_{\mathrm{demag}} - \mathbf{m}\cdot\mathbf{h}_{\mathrm{ext}}\right]\mathrm{d}v \tag{5}$$

where A is the exchange stiffness, μ_0 is the vacuum permeability, $\mathbf{h}_{\mathrm{ext}}$ is the external magnetic field, $\mathbf{h}_{\mathrm{demag}}(i,j,k) = \sum_{l,m,n} K(l,m,n)\mathbf{m}(i-l, j-m, k-n)$ is the magnetostatic field calculated using a GPU-accelerated fast Fourier transform and the convolution theorem, and $K(l,m,n)$ is the demagnetization tensor[58]. The magnetic parameters for the Py disk (30 nm thick, 1 μm diameter) are as follows: A = 13 pJ m^{-1}, M_s = 800 kA m^{-1}, α = 0.04 and mesh size $n_x \times n_y \times n_z = 5 \times 5 \times 5$ nm^3.

To integrate laser-induced photothermal demagnetization into the micromagnetic simulation, we used the semi-classical 3TM[49,59] to simulate the time-dependent temperature evolution of the electron (T_e), spin (T_s) and lattice (T_l) systems:

$$C_e(T_e)\frac{\mathrm{d}T_e}{\mathrm{d}t} = -G_{el}(T_e - T_l) - \mathrm{G}_{es}(T_e - T_s) + P(t) \tag{6}$$

$$C_s(T_s)\frac{\mathrm{d}T_s}{\mathrm{d}t} = -G_{es}(T_s - T_e) - \mathrm{G}_{sl}(T_s - T_l) \tag{7}$$

$$C_l(T_l)\frac{\mathrm{d}T_l}{\mathrm{d}t} = -G_{el}(T_l - T_e) - \mathrm{G}_{sl}(T_l - T_s) \tag{8}$$

where C_e, C_s, and C_l are the electron, spin and lattice heat capacity constants and G_{el}, G_{es} and G_{sl} are the electron–lattice, electron–spin and spin–lattice coupling constants (Supplementary Note 1). The parameters for Py used in the 3TM were reasonable, selected from within literature-reported ranges[39,60–62] such that the maximum spin temperature in the 3TM simulations remains close to, but does not exceed, the Curie temperature (see Supplementary Note 1 for details). The thermal boundary condition for the sample was implemented by considering the silicon nitride substrate as a thermal reservoir at a fixed temperature of 300 K. This treatment is physically reasonable, given that the dimensions of the silicon nitride substrate substantially exceed those of the Py disk, thus approximating an ideal heat sink. Considering that the laser pulse excitation in this experiment was well below the Curie temperature, the time-dependent spin temperature $T_s(t)$ can be scaled linearly using the experimentally determined $M_s(T)$ curves for Py (Supplementary Note 1). This approach allows time-dependent photothermal demagnetization $M_s(t)$ curves to be obtained without the need to include a temperature-dependent stochastic thermal fluctuating field acting on the atomistic local spin moment[63]. In this way, laser-induced dynamical micromagnetic simulations are achieved by incorporating $M_s(t)$ into the Landau–Lifshitz–Gilbert equation.

Data availability

The data that support the findings of this study are available from the corresponding authors upon reasonable request. Source data are provided with this paper.

References

57. Vansteenkiste, A. et al. The design and verification of MuMax3. *AIP Adv.* **4**, 107133 (2014).
58. Nobuo Hayashi, N. H., Koji Saito, K. S. & Yoshinobu Nakatani, Y. N. Calculation of demagnetizing field distribution based on fast fourier transform of convolution. *Jpn. J. Appl. Phys.* **35**, 6065 (1996).
59. Alber, L. et al. NTMpy: an open source package for solving coupled parabolic differential equations in the framework of the three-temperature model. *Comput. Phys. Commun.* **265**, 107990 (2021).
60. Mukhopadhyay, S. et al. Investigation of ultrafast demagnetization and Gilbert damping and their correlation in different ferromagnetic thin films grown under identical conditions. *Nanotechnology* **34**, 235702 (2023).
61. Ellis, M. O. A., Ostler, T. A. & Chantrell, R. W. Classical spin model of the relaxation dynamics of rare-earth doped permalloy. *Phys. Rev. B* **86**, 174418 (2012).
62. Panda, S. N. et al. Ultrafast demagnetization and precession in permalloy films with varying thickness. *Phys. Rev. B* **108**, 144421 (2023).
63. Khela, M. et al. Laser-induced topological spin switching in a 2D van der Waals magnet. *Nat. Commun.* **14**, 1378 (2023).

Acknowledgements

X.F. acknowledges support from the National Key Research and Development Program of China (grant no. 2020YFA0309300), the National Natural Science Foundation of China (NSFC) (grant nos 92477130, 12127803 and 12427806), the 111 Project (grant no. B23045) and the 'Fundamental Research Funds for the Central Universities' from Nankai University (grant nos ZB22000104, DK2300010207, 63243194 and 9242000728). R.E.D.-B. acknowledges support from the European Research Council under the European Union's Horizon 2020 Research and Innovation Programme (grant no. 856538). Z.H. acknowledges support from the Guangdong Basic and Applied Basic Research Foundation (grant no. 2023B1515020112) and the NSFC (grant nos 52322108 and 52271178). Z.L. acknowledges support from the National Key Research and Development Program of China (grant nos 2024YFA1408000 and 2023YFA1507000), the NSFC (grant no. 12304146) and the China Postdoctoral Science Foundation (grant nos 2023M741828 and 2024T170433). S.J. acknowledges support from the National Key Research and Development Program of China (grant no. 2023YFB3307700) and the aeronautical Science Foundation (grant no. 20240054OS6002). C.L. acknowledges support from Nankai University (grant no. 25NKSYJS04). W.H. acknowledges support from the NSFC (grant no. 12174427). This work was also supported by the Synergetic Extreme Condition User Facility (SECUF). Computations were supported by the Supercomputing Center of Nankai University.

Author contributions

X.F. conceived the research project. X.F. and C.L. performed the sample preparation. C.L., X.H. and X.F. carried out the in situ Lorentz transmission electron microscopy experiments. C.L., Z.L., X.H. and J.G. performed the experimental data analysis. W.H., T.G. and H.Z. performed the magnetometry measurements. Z.L. contributed to the theoretical model construction and numerical simulations. Z.L. and C.L. drafted the figures. Z.L., Z.H., C.L. and X.F. wrote the manuscript with input from Y.Z., R.E.D.-B. and D.Y. All authors contributed to the discussion and revision of the manuscript.

Competing interests

The authors declare no competing interests.

Additional information

Supplementary information The online version contains supplementary material available at https://doi.org/10.1038/s41565-026-02142-z.

Correspondence and requests for materials should be addressed to Dapeng Yu, Zhipeng Hou, Rafal E. Dunin-Borkowski, Yimei Zhu or Xuewen Fu.

Peer review information *Nature Nanotechnology* thanks the anonymous reviewers for their contribution to the peer review of this work.

Reprints and permissions information is available at www.nature.com/reprints.